Engineering of blended nanoparticle platform for delivery of mitochondria-acting therapeutics

Sean Marrache[a] and Shanta Dhar[a,b,1]

[a]Nano Therapeutics Research Laboratory, Department of Chemistry, and [b]Department of Physiology and Pharmacology, University of Georgia, Athens, GA 30602

Edited* by Robert Langer, Massachusetts Institute of Technology, Cambridge, MA, and approved August 24, 2012 (received for review June 13, 2012)

Mitochondrial dysfunctions cause numerous human disorders. A platform technology based on biodegradable polymers for carrying bioactive molecules to the mitochondrial matrix could be of enormous potential benefit in treating mitochondrial diseases. Here we report a rationally designed mitochondria-targeted polymeric nanoparticle (NP) system and its optimization for efficient delivery of various mitochondria-acting therapeutics by blending a targeted poly(D,L-lactic-*co*-glycolic acid)-block (PLGA-*b*)-poly(ethylene glycol) (PEG)-triphenylphosphonium (TPP) polymer (PLGA-*b*-PEG-TPP) with either nontargeted PLGA-*b*-PEG-OH or PLGA-COOH. An optimized formulation was identified through in vitro screening of a library of charge- and size-varied NPs, and mitochondrial uptake was studied by qualitative and quantitative investigations of cytosolic and mitochondrial fractions of cells treated with blended NPs composed of PLGA-*b*-PEG-TPP and a triblock copolymer containing a fluorescent quantum dot, PLGA-*b*-PEG-QD. The versatility of this platform was demonstrated by studying various mitochondria-acting therapeutics for different applications, including the mitochondria-targeting chemotherapeutics lonidamine and α-tocopheryl succinate for cancer, the mitochondrial antioxidant curcumin for Alzheimer's disease, and the mitochondrial uncoupler 2,4-dinitrophenol for obesity. These biomolecules were loaded into blended NPs with high loading efficiencies. Considering efficacy, the targeted PLGA-*b*-PEG-TPP NP provides a remarkable improvement in the drug therapeutic index for cancer, Alzheimer's disease, and obesity compared with the nontargeted construct or the therapeutics in their free form. This work represents the potential of a single, programmable NP platform for the diagnosis and targeted delivery of therapeutics for mitochondrial dysfunction-related diseases.

nanocarrier | organelle | nanomedicine | drug trafficking

Mitochondrial dysfunction is a key player in various human disorders, including cancer, neurodegenerative and neuromuscular diseases, obesity, and diabetes (1–3). One of the most challenging problems in the development of drug therapy to treat mitochondrial dysfunction is not the creation of the drugs themselves, but rather the distribution of these drugs to the mitochondria of cells (2). Drugs ranging from chemotherapeutics for cancer to antioxidants for Alzheimer's disease (AD) and uncouplers of oxidative phosphorylation for obesity act on the mitochondria of cells. However, clinical trials with mitochondria-acting therapeutics have failed to show benefits in humans owing to the logistics of safe drug delivery to the mitochondria in sufficient amounts and the toxicity associated with high doses.

The potential of nanoparticles (NPs) to improve any therapy lies in their ability to deliver payloads directly to the cells of interest and simultaneously enhance stability and pharmacokinetics. An equally important consideration is whether the same NPs can deliver the therapeutic payload to the intended target inside the cells. Delivery of payloads using biodegradable and Food and Drug Administration (FDA)-approved poly(lactic-*co*-glycolic acid) (PLGA)-based NPs to the target tissue has been well defined and characterized (4–6), but the intracellular barriers that delivery vehicles must overcome to reach subcellular target sites are less well understood. Several NP-based therapeutics are in clinical use for treating nonmitochondrial diseases (4), but NPs for mitochondrial dysfunction-associated diseases are still in their infancy (7). The development of technologies for targeted delivery of known mitochondria-acting therapeutics to the site of mitochondria has the potential to launch new therapeutic approaches for mitochondria-related diseases (8). Currently, only a handful of metal oxide- or liposomal-based carriers are known to deliver payloads to the mitochondria of cells (*SI Appendix*, Table S1) (9–17), none of which has demonstrated optimization and application of the FDA-approved biodegradable PLGA-based NP system in delivering known mitochondria-acting therapeutics to their precise destination.

In this report, we describe an engineering approach to the design and execution of a polymer-blending technology (18) to fine-tune size and surface charges of the resultant NPs to provide an optimized PLGA-based NP platform for mitochondria-targeted delivery of therapeutics. Incorporation of polyethylene glycol (PEG)-based polymer on the surface of PLGA-NPs results in longer blood circulation time (19). We synthesized a PLGA-*b*-PEG copolymer with a single terminal lipophilic triphenylphosphonium (TPP) cation, which is known to cross into the mitochondrial matrix space (20), to determine how the attached cation and variations in NP size and charge affect intracellular trafficking of blended NPs formed by mixing PLGA-*b*-PEG-TPP with either PLGA-*b*-PEG-OH or PLGA-COOH (Fig. 1 *A* and *B*). To demonstrate the wide application of our engineered NPs, we used a variety of mitochondria-acting therapeutics (8) used in AD (21), obesity (22), and cancer chemotherapy (23) as payloads. We chose curcumin, an inhibitor of amyloid-β protein (Aβ), for AD (24, 25); the mitochondrial decoupler 2,4-dinitrophenol (2,4-DNP) as an antiobesity drug (21); and lonidamine (LND), which inhibits mitochondrial glycolysis (26), and α-tocopheryl succinate (α-TOS), a tumor-selective drug, for cancer (27) (Fig. 1*B*).

Results and Discussion

Development of Targeted Blended NPs. Advances in understanding the importance of size, shape, and surface charge of PLGA-based NPs for mitochondrial uptake have the potential of creating opportunities for the development of targeted delivery vehicles for mitochondrial dysfunction-related diseases. We blended a mitochondrial-targeting functionalized polymer, PLGA-*b*-PEG-TPP, with PLGA-COOH or with PLGA-*b*-PEG-OH to vary the size and surface charge of the resultant NPs, to study the effect of these properties on the mitochondrial uptake and determine an optimal formulation. The likelihood of variation in NP properties increases with the number of processing steps required for synthesis. We anticipated that incorporating the TPP targeting moiety in the polymer before NP synthesis would minimize

Author contributions: S.M. and S.D. designed research; S.M. performed research; S.M. contributed new reagents/analytic tools; S.M. and S.D. analyzed data; and S.M. and S.D. wrote the paper.

The authors declare no conflict of interest.

*This Direct Submission article had a prearranged editor.

[1]To whom correspondence should be addressed. E-mail: shanta@uga.edu.

This article contains supporting information online at www.pnas.org/lookup/suppl/doi:10.1073/pnas.1210096109/-/DCSupplemental.

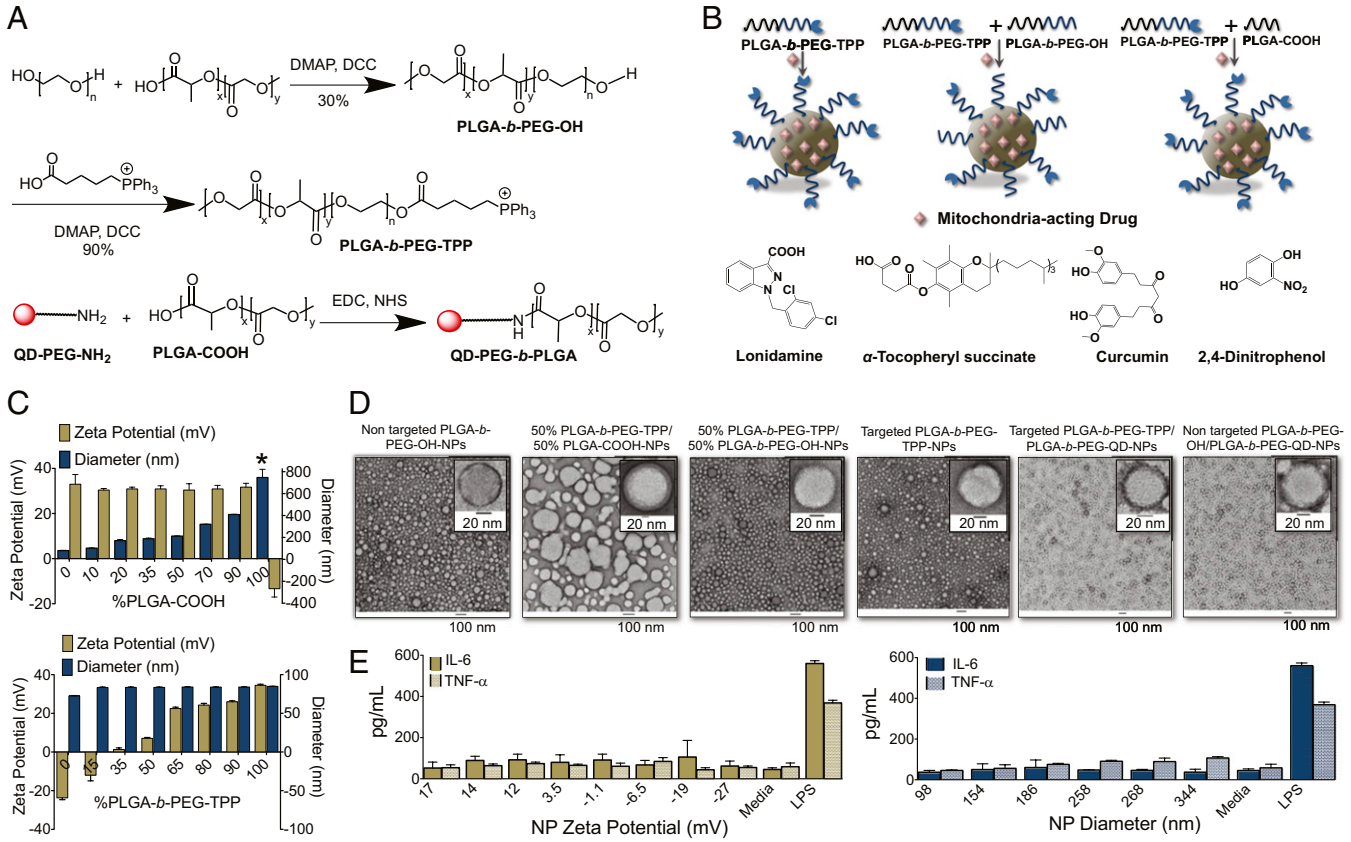

Fig. 1. (*A*) Synthesis of PLGA-*b*-PEG-OH, PLGA-*b*-PEG-TPP, and QD-conjugated polymer. (*B*) Construction of targeted and nontargeted NPs by blending PLGA-*b*-PEG-OH and PLGA-COOH with PLGA-*b*-PEG-TPP, with mitochondria-acting therapeutics used as payloads. (*C*) (*Upper*) Size and zeta potential variation in blended NPs from PLGA-*b*-PEG-TPP and PLGA-COOH. (*Lower*) Size and zeta potential variation in NPs by blending PLGA-*b*-PEG-TPP with PLGA-*b*-PEG-OH. (*D*) TEM images of targeted and nontargeted blended NPs. All of the TEM samples except the QD-blended NPs were negatively stained with sterile 2% (wt/vol) uranyl acetate aqueous solution for 15 min. (*E*) Secretion of IL-6 and TNF-α in the media with charge-varied and size-varied NPs (0.5 mg/mL) after 12 h. *NPs from 100% PLGA-COOH are unstable, and NP diameter varies from 700 nm to 10 μm depending on the batch preparation.

such variability. To deliver therapeutics inside the mitochondria with high efficiency, we synthesized a biodegradable polymer with a terminal OH group (PLGA-*b*-PEG-OH) to enable the conjugation of TPP to obtain PLGA-*b*-PEG-TPP (Fig. 1*A*). The conjugation of the targeting ligand affected the key properties of the NPs, including zeta potential, size, cellular uptake, and intracellular trafficking. We synthesized the blended NPs using a nanoprecipitation method (18, 28) (Fig. 1*B*), and obtained targeted and nontargeted blended NPs with reproducible diameter and surface charges in more than three independent nanoprecipitation experiments (*SI Appendix*, Table S2).

Optimization of NP Size and Charge for Mitochondrial Uptake. Optimizing the application of PLGA-based NPs as mitochondrial-targeted delivery vehicles requires a representative and comprehensive study addressing the effect of size and surface charge on the mitochondrial uptake. A crucial prerequisite to achieving this goal is the fabrication of NPs of different sizes and surface charges but with all other properties identical. We blended varying amounts of PLGA-COOH with PLGA-*b*-PEG-TPP to construct a library of NPs with varying size and constant surface charges. Using the blending technology, we were able to tune NP sizes from ∼80 to ∼410 nm (Fig. 1*C*; *SI Appendix*, Fig. S5 and Table S2) while keeping the number of TPP moiety constant, as evidenced by the constant surface charge (Fig. 1*C*). To explore the effect of surface charge on the mitochondrial uptake, we blended predefined amounts of PLGA-*b*-PEG-OH with PLGA-*b*-PEG-TPP. The surface charge was successfully altered without changing the main scaffold and NP size (Fig. 1*C*; *SI Appendix*, Fig. S6 and Table S2). These NP libraries exhibited homogenous populations of similar shape (TEM images; Fig. 1*D*), allowing us to explore the effects of NP size and charge on mitochondrial uptake.

Mitochondria-Targeting Properties. The cellular uptake profile of an NP system reflects the system's efficiency and bioavailability. Along with a quantitative evaluation of cellular uptake, subcellular location is of crucial importance for assessing the effectiveness of the current NP platform. We used a robust fluorescent reporter quantum dot (QD) to investigate the distribution of the targeted and nontargeted NPs in human cervical cancer HeLa cells. We used a QD-conjugated amine-terminated PEG, NH_2-PEG-QD, to track the NPs in the intracellular compartments. PLGA-COOH was conjugated to NH_2-PEG-QD to yield a triblock copolymer, PLGA-*b*-PEG-QD (Fig. 1*A*). We monitored the internalization of the targeted and nontargeted NPs by blending PLGA-*b*-PEG-QD with PLGA-*b*-PEG-TPP and with PLGA-*b*-PEG-OH, respectively. Confocal microscopy analysis of the treated cells indicated significantly greater uptake of targeted NPs than of nontargeted NPs in the mitochondria of cells (Fig. 2*A*). The details of the experimental procedure are described in the *SI Appendix*. A comparison of fluorescence intensities indicated a significantly greater overall uptake of the positively charged targeted NPs compared with nontargeted NPs. Quantitative analysis using the ImageJ "colocalization finder" plug-in revealed significant colocalization of the targeted NPs with MitoTracker Green (Invitrogen) in the mitochondria of cells (Pearson's correlation coefficient, $\rho = 0.53$; *SI Appendix*, Fig. S7).

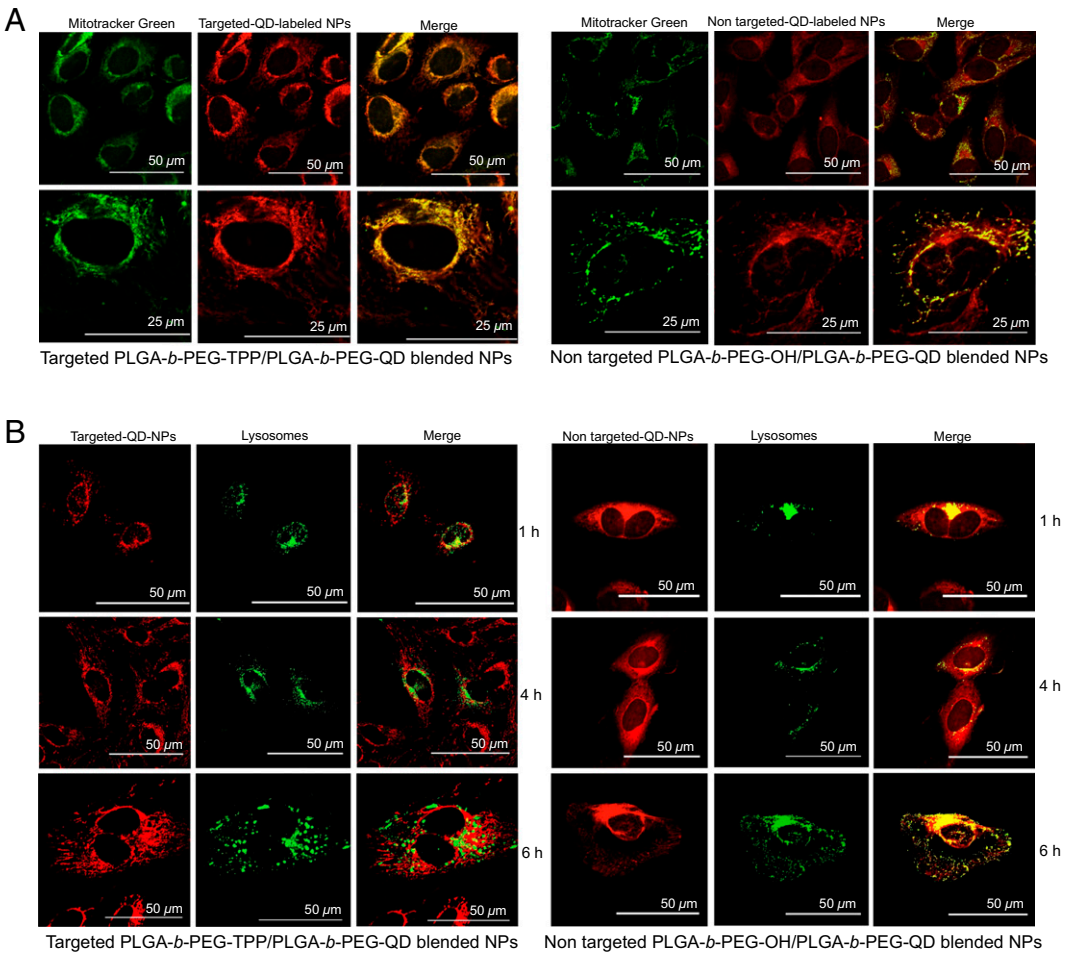

Fig. 2. (*A*) Subcellular localization of red fluorescent-targeted PLGA-*b*-PEG-TPP/PLGA-*b*-PEG-QD and nontargeted PLGA-*b*-PEG-OH/PLGA-*b*-PEG-QD blended NPs. HeLa cells were exposed to targeted NPs (diameter, 79 nm; zeta potential, 27.4 mV) and nontargeted NPs (diameter, 79 nm; zeta potential, −26.5 mV) at 10 μM or left untreated for 4 h. The cells were then stained with the mitochondrial marker MitoTracker Green (Invitrogen), fixed, and observed by wide-field fluorescence microscopy. The merged images and higher-magnification images show effective overlap of mitochondrial staining (green) and targeted NPs (red). No significant overlap was observed with nontargeted NPs. (*B*) Confocal images of time-dependent uptake of targeted PLGA-*b*-PEG-TPP/PLGA-*b*-PEG-QD blended NPs and nontargeted PLGA-*b*-PEG-OH/PLGA-*b*-PEG-QD blended NPs in HeLa cells. Lysosomes were stained with CellLight lysosomes-GFP, BacMam 2.0 (Life Technologies) (green).

With the nontargeted NPs, the red signals of the NPs and the mitochondrial staining differed in position, as demonstrated by a lower ρ value ($\rho = 0.03$).

Endosomal and Lysosomal Escape Properties. The uptake and intracellular trafficking of NPs occurs along several competing pathways. The use of NPs to target mitochondria is often limited by the fact that the NPs are taken up by the endosomal pathway, and that endosomes serve as a barrier to mitochondrial trafficking. We performed a time-dependent uptake study using the early endosome marker EAA-1 to investigate the fusogenic character necessary for efficient endosomal escape of the targeted NPs. The immunofluorescence procedure is described in detail in *SI Appendix*. For the targeted NPs, colocalization with endosomes was observed in the first hour and was decreased by 2 h (*SI Appendix*, Fig. S8). Over time, the targeted NPs exhibited complete endosomal escape and localized in the mitochondria of cells (Fig. 2*A*); however, significant colocalization with the early endosomes was observed with the nontargeted NPs even after 4 h (*SI Appendix*, Fig. S8). The highly efficient endosomal escape of the targeted NPs can be attributed to these NPs' high buffering capacity, which causes them to act as "proton sponges" (29). Proton absorbance by buffering of positively charged PEG prevents acidification of endosomal vesicles, thereby increasing the ATPase-mediated influx of protons and counter ions, which in turn leads to osmotic swelling, endosomal membrane rupture, and eventual leakage of the NPs into the cytosol, making them accessible for mitochondrial uptake.

To further support the findings that our NPs have high endosomal escapability and that some of the targeted NPs are not engaged in trafficking to lysosomes, we studied a time-dependent colocalization of the NPs with lysosomes (Fig. 2*B*). For the targeted NPs, colocalization with lysosomes decreased over time, suggesting lysosomal escape ability, whereas the nontargeted NPs were distributed in both the lysosomes and the cytoplasm.

Stability and Immunologic Effect of the Optimized NP Platform. Various positively charged NPs demonstrate interactions with serum proteins, causing aggregation owing to the surface adsorption of negatively charged proteins. Serum proteins had no effect on the size and polydispersity index (PDI) of our targeted NPs on incubation with 10% (vol/vol) FBS in DMEM or 10% (vol/vol) FBS in H_2O for 7 d (*SI Appendix*, Fig. S9). This finding was further supported by the observation that zeta potentials of the targeted NPs changed only minimally after contact with 10% FBS in DMEM or H_2O for 7 d, with no visible aggregation of particles (*SI Appendix*, Fig. S9). These findings suggest that the

excellent stability of the targeted NPs in serum makes them suitable for in vivo application.

This engineered NP platform can be used to transport therapeutics for in vivo application only if they do not trigger an immune response. Immune cells in the bloodstream and in tissues have a propensity to engulf and eliminate positively charged NPs. We evaluated immune responses from size- and charge-varied NPs in terms of the production of proinflammatory cytokines IL-6 and TNF-α in RAW 264.7 macrophages by ELISA, with LPS used as a control. The charge-varying NPs did not exhibit a pronounced immune response; however, NPs of >200 nm diameter demonstrated TNF-α production (Fig. 1*E*). These findings confirm that NPs of suitable size and charge are nonimmunogenic and can be used in systemic in vivo studies.

Quantification of Targeted NPs in Subcellular Compartments. To cross the mitochondrial membranes, NPs are transported across the outer membrane through the general import pore. We anticipated that the complicated structures of the tubular, vesicular, and flat cristae and their slight connections to the inner mitochondrial membrane might impose constraints on NP mobility and make their diffusion a very complicated, size-dependent process. The inner membrane potential ($\Delta\Psi_m$), which is negative on the inside, plays a major function in import by exerting an electrophoretic effect on the positively charged species. NPs with a high positive charge are expected to be imported at a lower $\Delta\Psi_m$ than NPs with a lower positive charge; thus, using a HeLa model cell line, we performed a comparative evaluation of the effect of NP size and charge in crossing the mitochondrial inner membrane (Fig. 3 *A*–*D*). We treated HeLa cells with targeted PLGA-*b*-PEG-TPP/PLGA-*b*-PEG-QD blended NPs of different sizes but similar zeta potential (*SI Appendix*, Fig. S10), then performed a quantitative investigation using inductively coupled plasma mass spectrometry (ICP-MS) to estimate the amount of cadmium (Cd) from the QDs internalized by the cells. Evaluation of the mitochondrial uptake of NPs of 80–330 nm diameter showed a trend toward a maximum uptake of 80- to 100-nm-diameter particles. Histograms showing the number of NPs in the cytosolic and mitochondrial fractions versus NP size indicate that the cellular uptake of NPs is heavily dependent on particle size (Fig. 3 *A* and *B*). We studied the effect of NP surface charge on cellular and mitochondrial uptake using a library of NPs with varying surface charges but similar hydrodynamic diameters (*SI Appendix*, Fig. S11), and detected no mitochondrial uptake (Fig. 3*C*) and very little overall cellular uptake (Fig. 3*D*) of negatively charged NPs. Cellular uptake increased as the surface charge reached 1.3 mV and remained constant up to a surface charge of ~22 mV, with increased mitochondrial uptake. We found another jump in cellular uptake as the surface charge increased to ~34 mV and reached saturation. Mitochondrial uptake increased significantly with the more positively charged NPs. This systematic investigation of the effect of NP diameter and surface charge may be useful in the design of optimized NP platforms for mitochondrial trafficking.

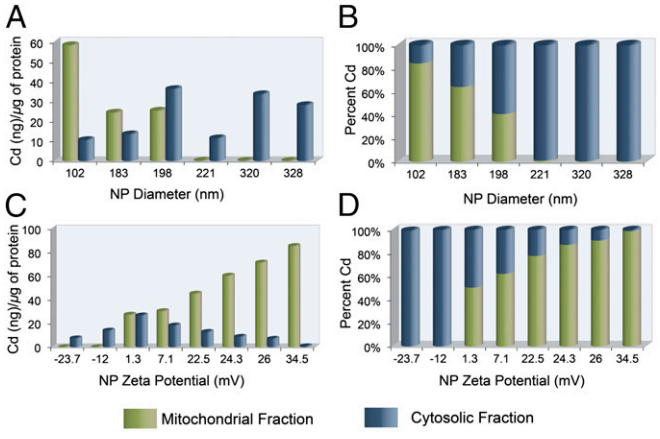

Fig. 3. Mitochondrial and cytosolic distribution of targeted PLGA-*b*-PEG-TPP/PLGA-*b*-PEG-QD blended NPs in HeLa cells by ICP-MS analysis. (*A*) Effect of size on uptake of NPs. (*B*) Overall cellular uptake of size-varying NPs. (*C*) Effect of zeta potential on cellular trafficking of NPs. (*D*) Overall cellular uptake of zeta potential-varying NPs.

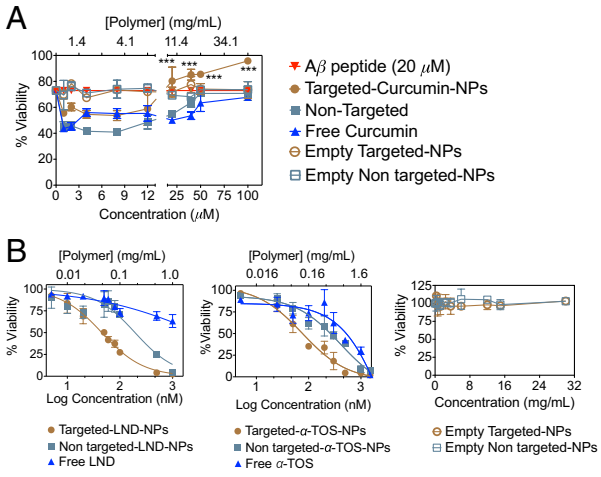

Fig. 4. (*A*) Effect on percent survival of IMR-32 neuroblastoma cells after treatment with targeted curcumin NPs, nontargeted curcumin NPs, and free curcumin against Aβ-induced cytotoxicity. The asterisk represents significant differences between targeted curcumin NPs, nontargeted curcumin NPs, and free curcumin according to one-way ANOVA with Tukey's post hoc test; $P < 0.001$. (*B*) Cytotoxicity profiles of targeted LND NPs, nontargeted LND NPs, free LND, targeted α-TOS NPs, nontargeted α-TOS NPs, free α-TOS in HeLa cells, empty targeted NPs, and empty nontargeted NPs in HeLa cells.

Delivery of Therapeutics to Dysfunctional Mitochondria. As a proof-of-concept demonstration of versatility of this system, we studied the delivery of mitochondria-acting therapeutics for the management of neurodegeneration, obesity, and cancer. We synthesized targeted and nontargeted NPs loaded with therapeutics with high loading and encapsulation efficiency using the nanoprecipitation method (*SI Appendix*, Table S3 and Figs. S12 and S13).

Application in Neurodegenerative Diseases. Amyloid-like plaques define the neuropathology of AD. Aggregations of the Aβ peptide form amyloid-like lesions, and thus reduction of amyloid burden by preventing Aβ formation represents an attractive approach to improving the therapeutic arsenal for AD. Curcumin is known to inhibit Aβ and the associated mitochondrial oxidative stress; however, its low bioavailability and photodegradation are major concerns. With such issues in mind, we formulated targeted curcumin-loaded NPs to provide photostability and enhance mitochondrial uptake. An in vitro survival evaluation of human neuroblastoma IMR-32 cells treated with 20 μM Aβ using the MTT [3-(4,5-dimethylthiazole-2-yl)-2,5-diphenyltetrazolium bromide] assay demonstrated enhanced neuroprotection with the targeted curcumin NPs compared with the nontargeted curcumin NPs or free curcumin (Fig. 4*A*) against Aβ, which accounts for the targeted delivery of curcumin to the mitochondria of cells.

Application in Cancer Chemotherapy. Mitochondria have emerged as a specific target for cancer treatment. Mitochondria-acting LND and α-TOS were selected to demonstrate the applicability of our system in cancer. The selectivity and efficiency of LND and α-TOS against cancer cells depend on their ability to target the mitochondria of cells. To evaluate the efficacy of our tar-

geted NPs in delivering LND and α-TOS, we performed MTT assays in HeLa cells, as described in *SI Appendix*. The IC_{50} value for targeted LND NPs was ∼5-fold lower than that for nontargeted NPs and 108-fold lower than that for free-form (Fig. 4*B* and *SI Appendix*, Table S4), indicating a greater cytotoxic effect. A greater cytotoxic effect also was observed with targeted α-TOS NPs compared with nontargeted α-TOS NPs and free α-TOS (IC_{50} 75 ± 2 nM, 230 ± 4 nM, and 381 ± 5 nM, respectively) (Fig. 4*B* and *SI Appendix*, Table S4). Preferential localization in the target organelle accounts for the enhanced cytotoxicity of both LND and α-TOS encapsulated in the targeted NPs. Our finding of no cytotoxic effect of the empty PLGA-*b*-PEG-TPP NPs even at high concentrations rules out a contribution of the delivery system and/or high zeta potentials to any cellular toxicity (Fig. 4*B*).

Possible Application in Obesity. Obesity has become a global health problem owing to its association with various metabolic disorders, including type 2 diabetes, cardiovascular diseases, and certain types of cancer. Because of the limited efficacy and undesirable side effects associated with the currently available antiobesity medications, attention has been focused on developing delivery vehicles that can directly deliver drugs to subcellular sites to modulate energy metabolism. The notable success of the mitochondrial uncoupler 2,4-DNP as a treatment for human obesity demonstrates that the beneficial effect of uncoupling on energy expenditure is not overwhelmed by compensatory increases in caloric intake. However, 2,4-DNP's narrow therapeutic window led to the abandonment of its use. A recent study found that 2,4-DNP linked to TPP in a covalent manner is ineffective at uncoupling (30). Concerns about the narrow therapeutic window and failure of the covalently linked uncoupler have led to the evaluation of mitochondria-targeted NPs in directing this uncoupler to the mitochondria of cells. To examine whether encapsulation of 2,4-DNP in targeted NPs can suppress the induced differentiation of 3T3-L1 preadipocytes at a low dosage that is insufficient to exert cytotoxicity, we continuously exposed 3T3-L1 cells to 1 μM, 4 μM, 25 μM, and 100 μM targeted 2,4-DNP NPs (Fig. 5 and *SI Appendix*, Fig S14) during the differentiation period for 7 d, and evaluated cell viability and intracellular lipid accumulation. Nontargeted 2,4-DNP NPs and free 2,4-DNP were used as controls. The presence of 1 μM, 4 μM, or 100 μM targeted 2,4-DNP NPs for 7 d during the differentiation period did not influence cell viability, but did produce a significant reduction in lipid accumulation compared with the nontargeted 2,4-DNP NPs or free 2,4-DNP (Fig. 5). Free 2,4-DNP at a concentration of 100 μM demonstrated cellular toxicity. These results indicate that 2,4-DNP in the targeted NPs can suppress the adipocytic differentiation of 3T3-L1 cells at a low concentration (1 or 4 μM) and do not exert a cytotoxic effect on these cells. We demonstrated that 2,4-DNP can be delivered to the mitochondria of cells using a targeted polymeric NP system to reduce lipid accumulation at a lower dose compared with the free form for possible application in the management of obesity.

Conclusion

In this proof-of-concept study, we have demonstrated that a suitably engineered mitochondria-targeted biodegradable PLGA-based NP delivery system can be made to enter the mitochondria of cells with high efficacy by fine-tuning NP surface charge and size. Not all types of NPs have the ability to enter mitochondria, because they cannot cross the complex double membrane owing to restrictions in programming surface charge and size. No previous report has examined the relationship between NP size and charge for efficient import to the mitochondria. This rationalized study addressing the effects of surface charge and diameter on the intracellular trafficking of PLGA-based NPs provides a generalized approach to the design of biodegradable nanocarriers for application in mitochondrial delivery. These targeted NPs can be used in various mitochondrial dysfunction-related disorders, including AD, obesity, and cancer. This work highlights several exceptionally promising research directions and provides a platform for diverse applications of PLGA-based NPs that can be integrated for imaging and therapy of mitochondrial dysfunction-related disorders.

Methods

Synthesis of PLGA-*b*-PEG-TPP. HO-PEG-OH (0.75 g; 0.23 mmol), PLGA-COOH (0.50 g; 0.1 mmol), and 4-dimethylaminopyridine (0.01 g; 0.08 mmol) were dissolved in 7 mL of dry CH_2Cl_2. A 2-mL CH_2Cl_2 solution of N,N′-dicyclohexycarbodiimide (DCC) (0.02 g; 0.1 mmol) was added dropwise to the reaction mixture at 0 °C with stirring. The mixture was warmed to room temperature and stirred overnight. Insoluble dicyclohexylurea was filtered, and the mixture was precipitated from 50 mL of 50:50 diethyl ether and methanol. The resulting solid was centrifuged at 1,400 × *g* for 15 min at 4 °C. As a final purification, a methanolic solution of PLGA-*b*-PEG-OH was precipitated repeatedly, washed with cold diethyl ether, and isolated as a white solid in a 30% (0.2 g) yield. ^{1}H-NMR ($CHCl_3$-*d*) (*SI Appendix*, Fig. S1): δ 5.3 [m, (O*CH*CH_3C(O)], 4.9 [m, (OCH_2C(O))], 3.6 [s, (OCH_2)], 1.9 [m, (CH_3CH)]. ^{13}C-NMR ($CHCl_3$-*d*) (*SI Appendix*, Fig. S1): δ 169.6, 166.5, 66.0, 61.1, 60.9, 16.89, 15.46. Gel permeation chromatography (*SI Appendix*, Fig. S4): M_n = 6,900 g/mol, M_w = 9,200 g/mol, M_z = 12,300 g/mol, PDI = 1.33. PLGA-*b*-PEG-OH (0.29 g; 0.03 mmol). (5-carboxypentyl)triphenylphosphonium cation (31) (0.11 g; 0.29 mmol), and 4-dimethylaminopyridine (0.007 g; 0.06 mmol) were dissolved in 3 mL of dry CH_2Cl_2. DCC (0.06 g; 0.29 mmol) was dissolved in CH_2Cl_2 (1 mL) and added dropwise to the reaction mixture at 0 °C with stirring. The mixture was stirred overnight at room temperature, after which any dicyclohexylurea formed was filtered off. Then 50 mL of cold diethyl ether was added to the resulting mixture to precipitate the polymer. The solid was centrifuged at 1,400 × *g* for 15 min at 4 °C. The solvent was removed, and the solid was lyophilized. The polymer was isolated as a white solid in 99% (0.3 g) yield. ^{1}H-NMR ($CHCl_3$-*d*) (*SI Appendix*, Fig. S2): δ 7.9–7.6 [m, 15H (Ar)], 5.3 [m, (O*CH*CH_3C(O)], 4.9 [m, (OCH_2C(O))], 3.6 [s, (OCH_2)], 1.9 [m, (CH_3CH)]. ^{13}C-NMR ($CHCl_3$-*d*) (*SI Appendix*, Fig. S2): δ 166.5, 135.3, 133.9, 130.7, 66.0,

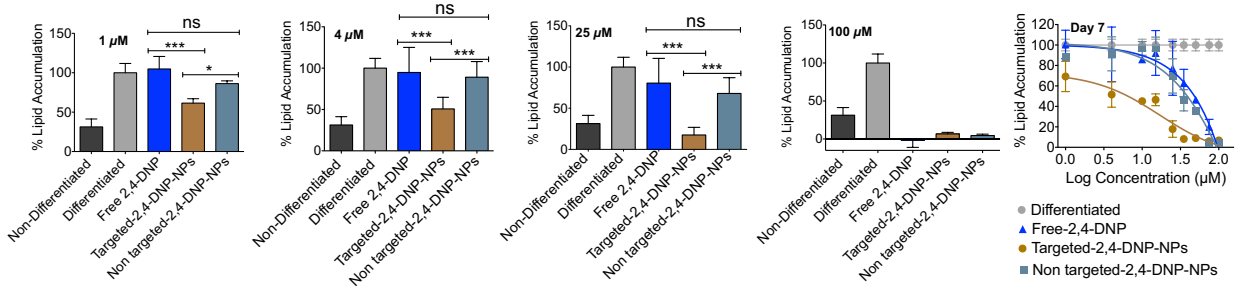

Fig. 5. Mouse 3T3-L1 preadipocytes were differentiated into adipocytes in the presence of 1 μM, 4 μM, 25 μM, or 100 μM of targeted 2,4-DNP NPs, nontargeted 2,4-DNP NPs, and free 2,4-DNP for 7 d. Nondifferentiated cells and completely differentiated cells were used as controls. Intracellular lipids were stained with AdipoRed (Lonza), and percent lipid accumulation was calculated. Inhibition of adipocyte differentiation is shown for day 7. Statistical analyses were performed using one-way ANOVA with Tukey's post hoc test. *$P < 0.05$; ***$P < 0.001$. Similar results were obtained from two independent experiments. ns, nonsignificant.

61.0, 16.89, 15.46. IR: ν cm^{-1} 3,029 (C-H sp^2), 2,944 (C-H sp^3), 2,200–2,000 (C-H Ar), 1,741 (C = O). ^{32}P-NMR ($CHCl_3$-*d*) (*SI Appendix*, Fig. S3): δ 24.37.

Synthesis of PLGA-*b*-PEG-QD. PLGA-COOH (0.4 g; 80 μmol), 1-ethyl-3-(3-dimethylaminopropyl) carbodiimide (EDC) (12.4 mg; 80 μmol), and NHS (9 mg; 80 μmol) were dissolved in 3 mL of dimethylformamide (DMF), and a 250-μL solution of 8 μM QD-PEG-NH_2 was added. The mixture was stirred at room temperature for 24 h, then filtered through a 100-kDa cutoff Amicon filter (Millipore). The resulting solid was dissolved in H_2O, lyophilized overnight, and then resuspended in DMF. PLGA-*b*-PEG-QDs were characterized using dynamic light scattering (DLS), which gave a hydrodynamic diameter of 10.1 ± 0.1 nm and a PDI of 0.3.

Synthesis of Targeted and Nontargeted NPs. NPs were synthesized by the nanoprecipitation method (18, 28). In brief, PLGA-*b*-PEG-OH or PLGA-*b*-PEG-TPP in acetonitrile to a final polymer concentration of 5 mg/mL was added dropwise to nanopure water with constant stirring. The NPs were then stirred for 2 h. Organic solvent was removed by three washes and filtering through a 100-kDa cutoff Amicon filter (Millipore). The NPs were resuspended in nanopure water and stored at 4 °C until further use. DLS measurements were performed to determine NP size, PDI, and zeta potential. PLGA-*b*-PEG-TPP NPs with tunable sizes were synthesized by blending predefined ratios of PLGA-COOH (0, 10%, 20%, 35%, 50%, 70%, and 90%) with PLGA-*b*-PEG-TPP following the nanoprecipitation method (*SI Appendix*, Table S2 and Fig. S5). Surface charges of PLGA-*b*-PEG-TPP NPs were varied by blending predefined ratios of PLGA-*b*-PEG-TPP (0, 15%, 35%, 50%, 65%, 80%, 90%, and 100%) with PLGA-*b*-PEG-OH following the aforementioned nanoprecipitation method (*SI Appendix*, Table S2 and Fig. S6). QD-blended NPs were synthesized following this nanoprecipitation method using PLGA-*b*-PEG-OH or PLGA-*b*-PEG-TPP in DMF:acetonitrile (1:9 ratio) with PLGA-*b*-PEG-QD (10 mmol solution in DMF) to a final polymer concentration of 5 mg/mL. DLS measurements were performed to determine size, PDI, and zeta potential (*SI Appendix*, Figs. S10 and S11). All NPs were characterized using TEM. For the synthesis of therapeutics-loaded NPs, PLGA-*b*-PEG-OH or PLGA-*b*-PEG-TPP (50 mg/mL in DMF) was mixed with a predefined amount of therapeutics (10 mg/mL in DMF) and diluted with acetonitrile to a final polymer concentration of 5 mg/mL. This mixture was added dropwise to nanopure water with constant stirring following the nanoprecipitation method. DLS measurements were performed to determine size, PDI, and zeta potential (*SI Appendix*, Fig. S12). Drug loading and encapsulation efficiency were determined by dissolving the polymeric core and using HPLC to quantify the amount of the therapeutics in the NPs (*SI Appendix*, Fig. S13).

Quantification of NPs in the Intracellular Compartments. QD-blended NPs (10 μM) of varying sizes and zeta potentials were internalized in HeLa cells (1.5×10^7 cells) for 12 h. After internalization, the mitochondria and the cytosol were isolated using a mitochondria isolation kit for mammalian cells. The cytosolic and mitochondrial fractions were then analyzed for Cd concentration in the QD by ICP-MS. A bicinchoninic acid (BCA) assay was performed on the isolated mitochondrial and cytosolic fractions to calculate the amount of Cd per microgram of protein isolated.

Adipogenesis Assay. To induce adipogenesis, 3T3-L1 preadipocytes were plated on a 96-well plate at a density of 5,000 cells per well and grown to confluence. The antiadipogenesis properties of targeted and nontargeted NPs loaded with 2,4-DNP and free 2,4-DNP were evaluated by internalizing the NPs on day 1 of the adipogenesis assay. Also on day 1, cells were induced to differentiate in a differentiation DMEM media containing 10% FBS supplemented with 0.5 mmol 3-isobutyl-1-methylxanthine (IBMX), 0.5 μM dexamethasone, and 20 nM insulin. On day 3, the induction medium was replaced with insulin medium containing DMEM, 10% FBS, and 20 nM insulin. After 6 d of treatment, cells were analyzed for triglyceride accumulation using the AdipoRed (Lonza) assay following the manufacturer's instructions.

Statistics. All data are expressed as mean ± SD. Differences among targeted, nontargeted, and free drugs were assessed by one-way ANOVA. $P < 0.05$ was considered to indicate statistical significance.

ACKNOWLEDGMENTS. We thank Dr. Nagesh Kolishetti for helpful discussions, Dr. Srujana Rayalam for assistance with the adipogenesis study, and the College of Veterinary Medicine Cytometry Core Facility for confocal microscope. This work was supported by National Institutes of Health startup Grant (P30 GM 092378) to the University of Georgia (UGA), and by the Office of the Vice President for Research, UGA (S.D.).

1. Duchen MR (2004) Mitochondria in health and disease: Perspectives on a new mitochondrial biology. *Mol Aspects Med* 25:365–451.
2. Fulda S, Galluzzi L, Kroemer G (2010) Targeting mitochondria for cancer therapy. *Nat Rev Drug Discov* 9:447–464.
3. Galluzzi L, et al. (2010) Mitochondrial gateways to cancer. *Mol Aspects Med* 31: 1–20.
4. Peer D, et al. (2007) Nanocarriers as an emerging platform for cancer therapy. *Nat Nanotechnol* 2:751–760.
5. Dhar S, Gu FX, Langer R, Farokhzad OC, Lippard SJ (2008) Targeted delivery of cisplatin to prostate cancer cells by aptamer functionalized Pt(IV) prodrug-PLGA-PEG nanoparticles. *Proc Natl Acad Sci USA* 105:17356–17361.
6. Hrkach J, et al. (2012) Preclinical development and clinical translation of a PSMA-targeted docetaxel nanoparticle with a differentiated pharmacological profile. *Sci Transl Med* 4:128ra139.
7. Agemy L, et al. (2011) Targeted nanoparticle enhanced proapoptotic peptide as potential therapy for glioblastoma. *Proc Natl Acad Sci USA* 108: 17450–17455.
8. Weissig V, D'Souza GGM (2010) Mitochondria-targeted drug delivery. *Targeted Delivery of Small and Macromolecular Drugs*, eds Narang AS, Mahato RI (CRC Press, Boca Raton, FL), pp 255–273.
9. Boddapati SV, D'Souza GGM, Erdogan S, Torchilin VP, Weissig V (2008) Organelle-targeted nanocarriers: specific delivery of liposomal ceramide to mitochondria enhances its cytotoxicity in vitro and in vivo. *Nano Lett* 8:2559–2563.
10. Patel NR, et al. (2010) Mitochondria-targeted liposomes improve the apoptotic and cytotoxic action of sclareol. *J Liposome Res* 20:244–249.
11. Esumi K, Takei N, Yoshimura T (2003) Antioxidant potentiality of gold-chitosan nanocomposites. *Colloids Surface B* 32:117–123.
12. Esumi K, Houdatsu H, Yoshimura T (2004) Antioxidant action by gold-PAMAM dendrimer nanocomposites. *Langmuir* 20:2536–2538.
13. Wang LM, et al. (2011) Selective targeting of gold nanorods at the mitochondria of cancer cells: Implications for cancer therapy. *Nano Lett* 11:772–780.
14. Paunesku T, et al. (2007) Intracellular distribution of TiO_2-DNA oligonucleotide nanoconjugates directed to nucleolus and mitochondria indicates sequence specificity. *Nano Lett* 7:596–601.
15. Hikosaka K, Kim J, Kajita M, Kanayama A, Miyamoto Y (2008) Platinum nanoparticles have an activity similar to mitochondrial NADH:ubiquinone oxidoreductase. *Colloids Surf B Biointerfaces* 66:195–200.
16. Kajita M, et al. (2007) Platinum nanoparticle is a useful scavenger of superoxide anion and hydrogen peroxide. *Free Radic Res* 41:615–626.
17. Sharma A, et al. (2012) Design and evaluation of multifunctional nanocarriers for selective delivery of coenzyme Q10 to mitochondria. *Biomacromolecules* 13:239–252.
18. Kolishetti N, et al. (2010) Engineering of self-assembled nanoparticle platform for precisely controlled combination drug therapy. *Proc Natl Acad Sci USA* 107: 17939–17944.
19. Beletsi A, Panagi Z, Avgoustakis K (2005) Biodistribution properties of nanoparticles based on mixtures of PLGA with PLGA-PEG diblock copolymers. *Int J Pharm* 298: 233–241.
20. Smith RA, Porteous CM, Gane AM, Murphy MP (2003) Delivery of bioactive molecules to mitochondria in vivo. *Proc Natl Acad Sci USA* 100:5407–5412.
21. Blaikie FH, et al. (2006) Targeting dinitrophenol to mitochondria: Limitations to the development of a self-limiting mitochondrial protonophore. *Biosci Rep* 26:231–243.
22. Liu JK, et al. (2009) Targeting mitochondrial biogenesis for preventing and treating insulin resistance in diabetes and obesity: Hope from natural mitochondrial nutrients. *Adv Drug Deliv Rev* 61:1343–1352.
23. Wang F, Ogasawara MA, Huang P (2010) Small mitochondria-targeting molecules as anti-cancer agents. *Mol Aspects Med* 31:75–92.
24. Mulik RS, Mönkkönen J, Juvonen RO, Mahadik KR, Paradkar AR (2010) ApoE3-mediated poly(butyl) cyanoacrylate nanoparticles containing curcumin: Study of enhanced activity of curcumin against beta amyloid-induced cytotoxicity using in vitro cell culture model. *Mol Pharm* 7:815–825.
25. Ono K, Hasegawa K, Naiki H, Yamada M (2004) Curcumin has potent anti-amyloidogenic effects for Alzheimer's beta-amyloid fibrils in vitro. *J Neurosci Res* 75: 742–750.
26. Floridi A, et al. (1981) Lonidamine, a selective inhibitor of aerobic glycolysis of murine tumor cells. *J Natl Cancer Inst* 66:497–499.
27. Neuzil J, et al. (2007) Mitocans as anti-cancer agents targeting mitochondria: Lessons from studies with vitamin E analogues, inhibitors of complex II. *J Bioenerg Biomembr* 39:65–72.
28. Dhar S, Kolishetti N, Lippard SJ, Farokhzad OC (2011) Targeted delivery of a cisplatin prodrug for safer and more effective prostate cancer therapy in vivo. *Proc Natl Acad Sci USA* 108:1850–1855.
29. Sonawane ND, Szoka FC, Jr., Verkman AS (2003) Chloride accumulation and swelling in endosomes enhances DNA transfer by polyamine-DNA polyplexes. *J Biol Chem* 278: 44826–44831.
30. Chalmers S, et al. (2012) Selective uncoupling of individual mitochondria within a cell using a mitochondria-targeted photoactivated protonophore. *J Am Chem Soc* 134:758–761.
31. Deroose FD, Clercq PJD (1995) Novel enantioselective syntheses of (+)-biotin. *J Org Chem* 60:321–330.